

Herzberg-Teller Vibronic Coupling Effect on the Vibrationally-Resolved Electronic Spectra and Intersystem Crossing Rates of a TADF Emitter: 7-PhQAD

Sirong Lin^a, Zheng Pei^a, Bin Zhang^a, Huili Ma^{b,*} and WanZhen Liang^{a,*}

^a*State Key Laboratory of Physical Chemistry of Solid Surfaces, Fujian Provincial Key Laboratory of Theoretical and Computational Chemistry, and Department of Chemistry, College of Chemistry and Chemical Engineering, Xiamen University, Xiamen, Fujian 361005, P. R. China*

^b*Key Laboratory of Flexible Electronics & Institute of Advanced Materials, Nanjing Tech University, 30 South Puzhu Road, Nanjing 211816, P. R. China*

E-mail: iamhlma@njtech.edu.cn, liangwz@xmu.edu.cn

Abstract

Assessing and improving the performance of organic light-emitting diode (OLED) materials require quantitative prediction of rate coefficients for the intersystem crossing (ISC) and reverse ISC (RISC) processes, which are determined not only by the singlet-triplet energy gap and the direct spin-orbit coupling (SOC) at a thermal equilibrium position of the initial electronic state but also by the non-Condon effects such as the Herzberg-Teller vibronic coupling (HTVC) and the spin-vibronic coupling (SVC). Here we applied the time-dependent correlation function approaches to calculate the vibronic absorption and fluorescence spectra and

*To whom correspondence should be addressed

ISC and RISC rates of a newly synthesized multiple-resonance-type (MR-type) thermally activated delayed fluorescence (TADF) emitter, 7-phenylquinolino[3,2,1-de]acridine-5,9-dione (7-PhQAD), with inclusion of the Franck-Condon (FC), HTVC, and Duschinsky rotation effects. It is found that the experimentally-measured ISC rate of 7-PhQAD originates predominantly from the HTVC which increases the ISC rate by more than one order of magnitude while the HTVC effect on the vibronic spectra is negligible. The small discrepancy between the theoretical and experimental rates originates from the neglect of the second-order SVC and the inaccurate excited states calculated by the single-reference time-dependent density functional theory. This work provides a demonstration of what proportion of ISC and RISC rate coefficients of a MR-type TADF emitter can be covered by the contribution of HTVC, and opens design routes that go beyond the FC approximation for the future development of high-performance systems.

Introduction

The OLED, an organic optoelectronic device based on fluorescence or phosphorescence emitters, has been successfully applied in displays and lighting.¹⁻⁵ However, due to the limitation of spin statistics and the raising of exciton deactivation at high current density,^{6,7} OLED devices still have low quantum yields. To break through the limitation of spin statistics and achieve nearly 100% internal quantum efficiency (IQE), scientists have proposed two strategies, one is based on the “singlet-trapping” and the other is based on the “triplet-trapping”. The first strategy utilizes phosphorescence materials to convert the singlet excitons to triplet excitons through efficient intersystem crossing (ISC) induced by the strong spin-orbit coupling (SOC) effect, so as to emit light from the lowest triplet excited state. The second strategy utilizes the delayed fluorescence materials to convert the triplet excitons to singlet excitons through efficient reverse ISC (RISC) induced by thermal activation, so as to emit light from emissive singlet excited state. Upon careful exploitation of these strategies, near 100% IQE can be achieved.⁸ In this regard, the performance of OLED device is inseparable from the ISC and RISC processes. Therefore, it is of particular

importance for us to study the mechanism and quantitatively predict the rate coefficients. It is also essential to explore in depth what other factors besides the well-known singlet-triplet energy gap (ΔE_{ST}) and SOC matrix elements (SOCMEs) have an impact on the rate coefficients. Powerful computing resources and effective algorithms provide a way to resolve this challenge.^{9–12} One can gain a detailed insight into the mechanism of ISC and RISC processes through analysing the results of theoretical calculations.

Both the calculations of molecular vibronic spectra,^{13–22} and the ISC and RISC rate coefficients require us to account for simultaneous changes in the vibrational and electronic states. One thus needs to combine both the electronic structure theories and quantum dynamics methods to obtain the structure parameters and to describe quantum dynamics, respectively. The earliest research examples to characterize the vibronic properties were to calculate the phosphorescence of small aromatic hydrocarbons such as benzene.^{23–25} Later, the vibronic effects were involved in the calculations of ISC rates of some organic molecules.^{26–29} Many recent studies on TADF materials (e.g. Refs 30–35) demonstrated that the vibronic effect on the RISC rates is significant. The nonadiabatic couplings (NACs) between the low-lying excited singlet states and triplet states open the possibility for significant second-order coupling effects, and increase RISC rate by a few orders of magnitude in some TADF emitters.³⁰ So that, the quantitative predication of the ISC and RISC rates of a TADF emitter requires taking the vibronic states into account, rather than the pure electronic states.^{26,31}

The vibronic coupling effects on the S–T crossing rate coefficients should include both the contributions of HTVC and spin-vibronic coupling (SVC). Many previous works found that the second-order SVC (the last term of the right-hand side (RHS) of Eq. (6)) assisted triplet to singlet up-conversion, increasing RISC rates by a few orders of magnitude in some TADF emitters. They thus applied a full second-order SVC model to calculate S–T crossing rates (e.g. Refs 33,35,43). Usually, the second-order vibronic coupling effect in most cases is much smaller than the first-order one. However, due to a vibronic resonance that orchestrates three electronic states (S_1 , T_1 and T_2) together, $S_1 - T_2$ crossing plays a major role in enhancing ISC and RISC of some MR-type

TDAF emitters.^{33,42}

Li et al.³⁶ synthesized a narrow-band, ultrapure blue TADF material, 7-PhQAD, which is based on a rigid framework of quinolino-[3,2,1-*de*]acridine-5,9-dione. 7-PhQAD molecule's S_1 and T_1 states mainly possess (π , π^*) character leading to the transition of $S_1 \rightarrow T_1$ nearly spin forbidden according to El-Sayed's rule.³⁷ Nevertheless, the experimentally-measured ISC rate actually reaches 10^8 s^{-1} , indicating the significant impact of the vibronic coupling effects. Here we thus calculate the vibrationally-resolved absorption and fluorescence spectra as well as its ISC and RISC rates to verify the microscopic mechanism of TADF process. We aim to describe its photophysical properties, quantitatively predict the ISC and RISC rates, and unveil the mechanism of the singlet-triplet (S-T) intersystem crossings. The time-dependent correlation function approaches, which have been implemented by our group to calculate the electronic absorption and emission spectra and resonant Raman scattering spectra^{19,21,22} with including the Franck-Condon (FC), Herzberg-Teller vibronic coupling (HTVC)³⁸ and Duschinsky rotation (DR)^{39,40} effects, have been extended to calculate the ISC and RISC rates of 7-PhQAD emitter.

In our calculations of S-T crossing rates, we include FC and HTVC contributions and ignore the second-order SVC effect, a similar way with Refs. 12,41. It is that only the first two terms of SOCME in Eq.(6) are involved. It is well known that $\frac{\partial H_{SO}^i}{\partial Q_k}$ can be approximately written as $\sum_{m \neq i} \frac{H_{SO}^{fm} H_{mi,1}^k}{E_i - E_m} + \sum_{n \neq f} \frac{H_{fn,3}^k H_{SO}^{ni}}{E_f - E_n}$ based on the perturbed wavefunctions of the initial and final states, where $H_{er,\sigma}^k = \langle \sigma \Psi_e | \partial \hat{H}^{el} / \partial Q_k | \sigma \Psi_r \rangle = (E_r - E_e) \langle \sigma \Psi_e | \partial / \partial Q_k \sigma \Psi_r \rangle$. $\langle \sigma \Psi_e | \partial / \partial Q_k \sigma \Psi_r \rangle$ is defined as the NAC vector between two excited states of the given spin multiplicity σ . Therefore, the HT-type vibronically-induced term provides mixing of the triplet and singlet excited states being coupled by the first order vibronic perturbation due to the nuclear displacement along with the $3N - 6$ normal modes Q . Anyway, in this work, we account for the HTVC effect via directly evaluating the nuclear derivatives of SOC not via calculating NAC vectors between the excited states.

We aim to provide a demonstration of what proportion of ISC/RISC rate of a TADF emitter can be covered by the HT-type vibronic coupling effect.

Theoretical Methods and Computational Details

With respect to the Fermi-Golden rule,⁴⁴ the transition rate (k) from the initial state i to a dense manifold of final states f can be described as

$$k_i = \frac{2\pi}{\hbar} \sum_f |\langle \Phi_f | \hat{H}' | \Phi_i \rangle|^2 \delta(E_f - E_i \mp \hbar\omega), \quad (1)$$

where $|\Phi_i\rangle$ and $|\Phi_f\rangle$ are the wavefunctions of the initial and final vibronic states, respectively, ω is the frequency of the external radiation. \hat{H}' denotes the perturbation and can be written as $\hat{H}' = -\vec{\mu} \cdot \vec{f} + \hat{T}_N + \hat{H}_{SO}$, where the first, second and third operators separately correspond to the matter-field interaction, the nuclear kinetic energy, and spin-orbit interaction. The radiative transition like electronic absorption or emission is usually governed by the matrix element of $\langle \Phi_f | \hat{\mu} | \Phi_i \rangle$ while the nonradiative processes like internal conversions and ISCs or RISCs are determined by the matrix elements of later two operators. If we introduce the integral representation of the delta function $\delta(E_f - E_i \mp \hbar\omega) = \frac{1}{2\pi} \int_{-\infty}^{+\infty} e^{i(\frac{E_f - E_i}{\hbar} \mp \omega)t} dt$, and define $\hat{H}'(t) = e^{\frac{i\hbar t}{\hbar}} \hat{H}' e^{-\frac{i\hbar t}{\hbar}}$, the rate equation becomes

$$\begin{aligned} k_i &= \frac{1}{2\pi} \int_{-\infty}^{+\infty} \sum_f \langle \Phi_f | \hat{H}'(t) | \Phi_i \rangle \cdot \langle \Phi_i | \hat{H}' | \Phi_f \rangle e^{\mp\omega t} dt \\ &= \frac{1}{2\pi} \int_{-\infty}^{+\infty} \langle \Phi_i | \hat{H}' \cdot \hat{H}'(t) | \Phi_i \rangle e^{\mp\omega t} dt. \end{aligned} \quad (2)$$

For a S–T intersystem crossing, if we restrict ourselves to and second-order terms, the coupling matrix element can be expressed as^{25,45}

$$\begin{aligned} H'_{if} &= \langle {}^3\Phi_f | \hat{H}_{SO} | {}^1\Phi_i \rangle \\ &+ \sum_{m \neq i} [\langle {}^3\Phi_f | \hat{H}_{SO} | {}^1\Phi_m \rangle \langle {}^1\Phi_m | \hat{T}_N | {}^1\Phi_i \rangle / (E_i - E_m)] \\ &+ \sum_{n \neq f} [\langle {}^3\Phi_f | \hat{T}_N | {}^3\Phi_n \rangle \langle {}^3\Phi_n | \hat{H}_{SO} | {}^1\Phi_i \rangle / (E_f - E_n)], \end{aligned} \quad (3)$$

where the summations extend over the complete sets of pure-spin Born-Oppenheimer (psBO) states

of the given multiplicity. The first term is called as the direct SOC, and the last two terms originate from the mixed vibronic and SOC, usually called as the SVC. Although Eq. (3) specifically refers to a S \rightarrow T crossing, the corresponding expression for the reverse crossing is readily written down.

One may evaluate Eq. (3) by making use of the HT expansion, i.e., expand the integrals about the nuclear equilibrium configuration $Q = 0$. Writing the psBO functions as products of an electronic wavefunction Ψ and a vibrational wavefunction Λ like ${}^\sigma\Phi_n(q, Q) = {}^\sigma\Psi_n(q, Q)\Lambda_n(Q)$, we have

$${}^\sigma\Psi_n(q, Q) = {}^\sigma\Psi_n(q, 0) + [\partial{}^\sigma\Psi_n(q, 0)/\partial Q]_{Q=0} Q + \dots, \quad (4)$$

$$H_{SO}^{if} = H_{SO}^{if}|_{Q=0} + [\partial H_{SO}^{if}/\partial Q]_{Q=0} Q + \dots. \quad (5)$$

The second term in Eq. (5) originates from vibronically induced SOC or the HT expansion. If we terminate the expansions after the lowest-order nonvanishing term, H'_{if} in Eq. (3) can be written as^{25,45}

$$\begin{aligned} H'_{if} = & H_{SO}^{fi}|_{Q=0} \langle \Lambda_f(Q') | \Lambda_i(Q) \rangle + \sum_{k=1}^{3N-6} \left(\frac{\partial H_{SO}^{fi}}{\partial Q_k} \Big|_{Q=0} \langle \Lambda_f(Q') | Q_k | \Lambda_i(Q) \rangle \right) \\ & - \sum_{k=1}^{3N-6} \left(\left[\sum_{m \neq i} \frac{H_{SO}^{fm} H_{mi,1}^k}{(E_i - E_m)^2} + \sum_{n \neq f} \frac{H_{fn,3}^k H_{SO}^{ni}}{(E_f - E_n)^2} \right]_{Q=0} \langle \Lambda_f(Q') | \frac{\partial}{\partial Q_k} | \Lambda_i(Q) \rangle \right). \quad (6) \end{aligned}$$

If the first term, the direct SOC, vanishes, this intersystem crossing is spin forbidden. In the above derivative, we apply the relation of $\langle {}^\sigma\Phi_e | \hat{T}_N | {}^\sigma\Phi_r \rangle \sim -\sum_{k=1}^{3N-6} \langle {}^\sigma\Psi_e | \nabla_k | {}^\sigma\Psi_r \rangle \langle \Lambda_e(Q') | \nabla_k | \Lambda_r(Q) \rangle$.

In our calculations of S–T crossing rates, we only keep the first two terms of Eq. (6) and ignore the last second-order SVC term. If the harmonic oscillator approximation to the potential energy surfaces is adopted, then the calculations of S–T crossing rates are similar to the calculation of vibrationally-resolved absorption and fluorescence spectra. In the later cases, SOC operator is replaced by the dipole operator $\hat{\mu}$ and S₀ and S₁ states are concerned. We have implemented these time-dependent correlation function approaches to calculate the vibronic spectra including one- and two-photon absorption and emission^{20,21} and resonance Raman scattering spectra.¹⁹ A

summary of our previous works on the vibronic spectra has been given in Ref. 22. Here we extend this time-dependent approach to calculate the S–T crossing rates.

Within the adiabatic approximation the molecular Hamiltonian can be written as $\hat{H} = |\Psi_i\rangle\hat{H}_i\langle\Psi_i| + |\Psi_f\rangle(\hat{H}_f + \Delta E)\langle\Psi_f|$, where \hat{H}_i and \hat{H}_f are the vibrational Hamiltonians of the initial and final vibronic states, respectively. If we ignore the spin-vibronic interaction terms in H'_{if} , and account for the Boltzmann distribution of the initial-state vibronic manifold at the finite temperature and the molecular energy conservation for the nonradiative transition, i.e. $\omega = 0$, Eq. (2) becomes the following thermal rate constant form for the transition from the initial to the final electronic states

$$k(T) = \frac{1}{2\pi} \int_{-\infty}^{+\infty} dt e^{(i\Delta Et/\hbar + i\gamma t - \gamma^2/\beta)} C(t), \quad (7)$$

with $C(t) = \frac{\text{Tr}[e^{-\beta\hat{H}_i} H_{\text{SO}}^{if} e^{i\hat{H}_f t/\hbar} H_{\text{SO}}^{if} e^{-i\hat{H}_i t/\hbar}]}{\text{Tr}[e^{-\beta\hat{H}_i}]}$. Here $\beta = 1/k_{\text{B}}T$, $\text{Tr}(\dots)$ represents the trace over nuclear degrees of freedom, and H_{SO}^{if} denotes the SOCME between the initial and final electronic states, including the direct SOC and its derivative term as expressed in Eq. (5). ΔE is the energy difference between two concerned electronic states of $|\Psi_i\rangle$ and $|\Psi_f\rangle$ (0-0 transition). γ represents the solvent reorganization energy, and the corresponding exponential form of γ comes from the high temperature approximation of solvent mode.⁴⁶ A detailed derivation about the exponential expression of the γ has been given in supporting information (SI).

We calculate the SOCMEs between a pair of singlet and triplet electronic states at the theoretical level of the time-dependent density functional theory (TDDFT) within Q-Chem 5.2 software package.⁴⁷ The root-mean-square SOCME between a pair states is defined as

$$\langle {}^1\Psi_n | \hat{H}_{\text{SO}} | {}^3\Psi_m \rangle = \sqrt{\sum_{m_s=0,\pm 1} \|\langle {}^1\Psi_n | \hat{H}_{\text{SO}} | {}^3\Psi_m^{m_s} \rangle\|^2}. \quad (8)$$

The derivatives of the SOCMEs with respect to the nuclear coordinates have been calculated numerically using a three-point finite-difference approximation with a step length of 0.001 Å. Considering the three degenerate electronic substates of the triplet ($m_s = 0, \pm 1$), the calculated RISC rate is scaled by a factor of 1/3.

TADF emerges from a balance of charge-transfer (CT) and local excited states.^{48–52} The conventional approximate exchange-correlation functionals and kernels can lead to a large error in TDDFT calculations of a TADF emitter. The tuned range-separated XC functionals have thus been suggested to describe the excited-states properties with inclusion of CT character.^{53–57} Here we tuned the range-separation parameter ω by minimizing the function^{58,59} of $\sum_{i=0}^{i=1} [\epsilon_{\text{HOMO}}(\omega, N+i) + \text{IP}(\omega, N+i)]^2$, where ϵ_{HOMO} is the energy of the highest occupied molecular orbital (HOMO) and IP is the ionization energy.

Unless otherwise specified, the calculations involved in this article are carried out in toluene by using the polarizable continuum model with the integral equation formalism variant^{60–62} and at the theoretical level of (TD-)CAM-B3LYP* (* means ω has been tuned)/6-311++G** with the Tamm-Dancoff approximation (TDA).⁶³ The Multiwfn3.7 package^{64,65} is adopted to plot the MOs involved in the corresponding electronic excitations and the charge density differences between the corresponding excited states and ground state.

Results and Discussion

The geometric and electronic structures, and vibrationally-resolved absorption and fluorescence spectra

The geometric structure of 7-PhQAD molecule is shown in Figure 1.

In order to find out what effect other states may bring, at first we calculate the excitation energies of the low-lying excited states of 7-PhQAD by TDDFT with and without TDA. The conventional hybrid XC functional B3LYP,⁶⁶ and three optimally tuned range-separated XC functionals CAM-B3LYP*,⁶⁷ ω *B97X-D,^{68,69} and LC-BLYP*^{68,70} have been adopted. The calculated vertical and adiabatic excitation energies (VEEs and AEEs) are shown in Table 1. The experimentally-measure absorption and fluorescence maxima of 7-PhQAD in toluene are 446 nm (2.78 eV) and 464 nm (2.67 eV), respectively, and only a difference of 18 nm exists.³⁶ TDDFT slightly overestimates the absorption and emission energies, and significantly overestimate the energy gap of

Table 1: VEE and AEE in a unit of eV calculated by TDDFT with and without TDA and ADC(2), respectively. The oscillator strengths are shown in parenthesis.

States	B3LYP		CAM-B3LYP*		ω B97XD*		LC-BLYP*		ADC(2)	
	TDA	TDDFT	$\omega = 0.071$	$\omega = 0.071$	$\omega = 0.032$	$\omega = 0.032$	$\omega = 0.065$	$\omega = 0.065$		
VEEs	T ₁	2.40	2.36	2.40	2.36	2.51	2.47	2.07	2.06	2.92
	S ₁	2.94	2.86	2.96	2.87	3.06	2.98	2.54	2.46	3.19
		(0.25)	(0.20)	(0.26)	(0.20)	(0.27)	(0.22)	(0.20)	(0.15)	(0.1715)
	T ₂	3.07	2.95	3.07	2.95	3.16	3.03	2.49	2.48	3.14
	T ₃	3.09	3.04	3.10	3.04	3.18	3.13	2.67	2.65	3.25
	S ₂	3.38	3.37	3.39	3.38	3.47	3.46	2.70	2.69	3.36
	(0.00)	(0.0001)	(0.00)	(0.00)	(0.00)	(0.00)	(0.0024)	(0.0005)	(0.0003)	
AEEs	T ₁	2.30	2.26	2.31	2.21	2.41	2.37	1.99	1.98	
	T ₂	2.87	2.79	2.87	2.72	2.96	2.85	2.30	2.28	
	S ₁	2.86	2.78	2.88	2.73	2.98	2.89	2.46	2.38	3.04

$\Delta E_{S_1T_1}$ compared to the experimental energy gap of 1532 cm^{-1} (0.19 eV).³⁶ For example, the first three functionals produce the vertical and adiabatic energy gaps of ≥ 0.5 eV, and the LC-BLYP* yields a slightly smaller value of ~ 0.4 eV.

The appreciable overestimation to $\Delta E_{S_1T_1}$ by the single-reference TDDFT approach indicates that 7-PhQAD molecule is a strongly correlated system. To check this, we calculated VEEs of low-lying excited states using the algebraic-diagrammatic construction scheme of second order ADC(2).⁷¹ The correlation consistent basis set, cc-pVDZ, was adopted. ADC(2)/cc-pVDZ overestimates the absorption and emission energies (see Table S1 in SI), but produces an energy gap of 0.27 eV, which is much closer to the experimental gap of 0.19 eV. The double substitutions contribute 13% and 11% to S₁ and T₁ states, respectively, as Table S1 in SI shows, meaning that the failure of TDDFT approach is attributed to its single-reference character, and the multireference quantum chemistry methods are needed to exactly describe 7-PhQAD molecule.

The electronic excitations of S₀ \rightarrow S₁ and S₀ \rightarrow T₁ are dominated by HOMO \rightarrow LUMO transitions with a percentage of 95.1 and 96.1, respectively, evidenced by the nearly identical density differences shown in Figure S2. Both S₀ \rightarrow S₁ and S₀ \rightarrow T₁ transitions mainly have (π , π^*) and intramolecular CT characters as Figure 1 and Figure S2 in SI show. It can then be deduced that the

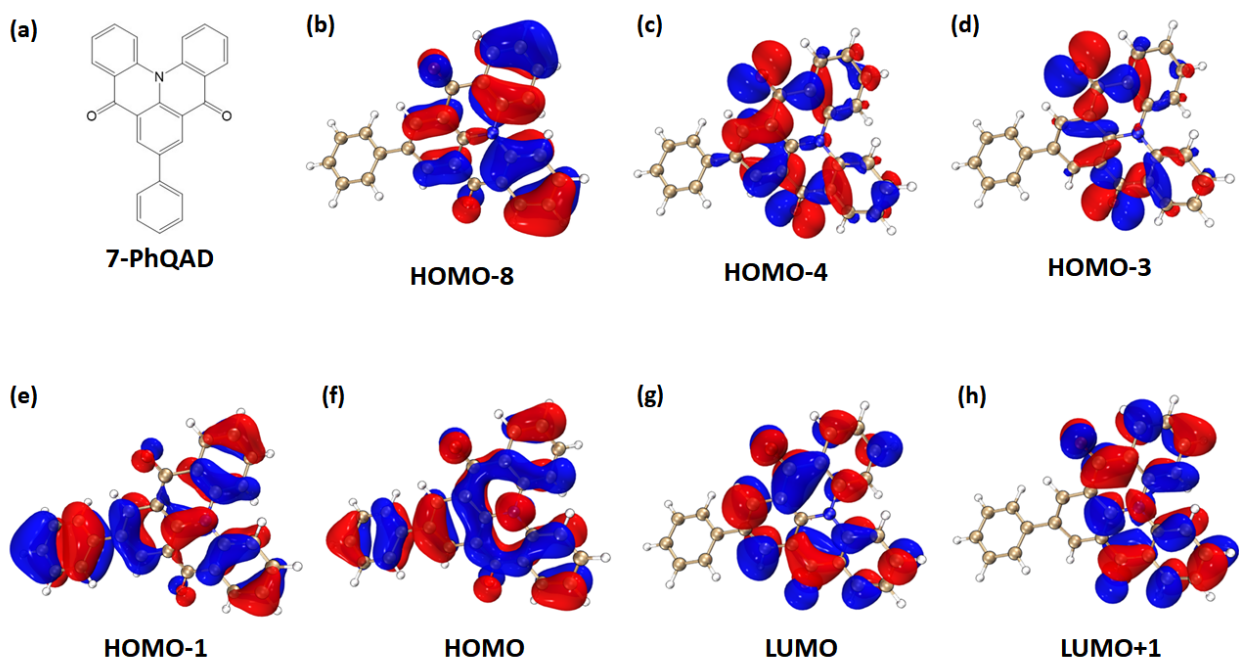


Figure 1: (a) The geometric structure of 7-PhQAD. (b-h) The primary MOs concerned with the electronic excitations. An isovalue of 0.02 au is applied.

SOCME between S_1 and T_1 is negligible small according to the El-Sayed's rule, verified by the calculated values shown in Table 2.

Unlike $S_0 \rightarrow S_1$ and $S_0 \rightarrow T_1$ excitations, more MO transitions contribute to T_2 and T_3 states. For $S_0 \rightarrow T_2$, HOMO-3 \rightarrow LUMO and HOMO-4 \rightarrow LUMO+1 contribute 74.0% and 11.3%, respectively. Consequently, T_2 state has the character of (n, π^*) . For $S_0 \rightarrow T_3$, HOMO \rightarrow LUMO+1 makes a major contribution, accounted for 55.1%, followed by HOMO-4 \rightarrow LUMO of 14.8%. As shown in panels (c) and (d) of Figure S2, the density difference plots of T_2-S_0 and T_3-S_0 show local excitation character, and are different from that of S_1-S_0 . As a result, the SOCMEs of S_1-T_2 and S_1-T_3 should be larger than that of S_1-T_1 .

According to the El-Sayed's rule, in order to compensate for the momentum change caused by electron spin reversal, it is necessary for an electron to jump in a mutually perpendicular orbit to balance the momentum change. Therefore, the initial and final states must have different transition properties to make ISC take place. But unfortunately, both S_1 and T_1 states of 7-PhQAD mainly have (π, π^*) character, indicating that if only direct SOC between S_1 and T_1 is considered, the ISC

is hard to happen. In terms of the calculated excitation energies, T_2 and even T_3 are in energy close to S_1 , and these states are almost degenerate, indicating that the population transition via S_1-T_n ($n>1$) may potentially play a crucial role in ISC and RISC processes.

Considering the intramolecular CT and (π , π^*) characters of the excited states, after comprehensive consideration, we use the optimally-tuned XC functional CAM-B3LYP* in the later calculations.

The calculated vibrationally-resolved absorption and fluorescence spectra are shown in Figure 2. In our calculations, the adiabatic energy gap between S_0 and S_1 states (0-0 transition) is set to be nearly same with the calculated value by TDA-CAM-B3LYP*. The theoretical calculation with the vertical gradient (VG) approximation^{21,40,72} produces a narrow-band absorption and emission with very small full-width at half-maximum (FWHM), which coincided with the experimental measurement. The spectral lineshapes indicate that this material possesses a rigid nature which can significantly reduce the vibrational motion to obtain narrow-band emission with very small FWHM. The VG approximation assumes that the S_1 potential energy surface (PES) is just a shifted PES of the S_0 , meaning that the electronic excitation doesn't change the shape of PES much. The theoretical calculation without VG approximation accounts for the difference between S_0 and S_1 PESs, and largely overestimates FWHM compared to the experimental value, attributed to the inaccurate S_1 PES calculated by the single-reference TDDFT. As the key geometrical parameters listed in Table S2 in SI show, TDDFT with and without TDA predicts a larger difference between the ground and excited-state geometries than ADC(2). TDDFT produces a more twisted conformation for S_1 state than ADC(2). The HTVC effect on the absorption and emission spectra is negligibly small.

Anyway, 7-PhQAD is relatively rigid, and the different types of electronic excitations from $S_0 \rightarrow S_1$ and $S_0 \rightarrow T_1$ don't alter its geometric structure much. The optimized geometrical structures of S_1 and T_1 only exhibit a slight difference in the dihedral angles between the benzene ring and the main body, which are 26.6° and 24.6° , respectively. The root mean square deviation (RMSD) between S_1 and T_1 geometric parameters is only 0.02 \AA (see Figure S3 in SI). The minimal

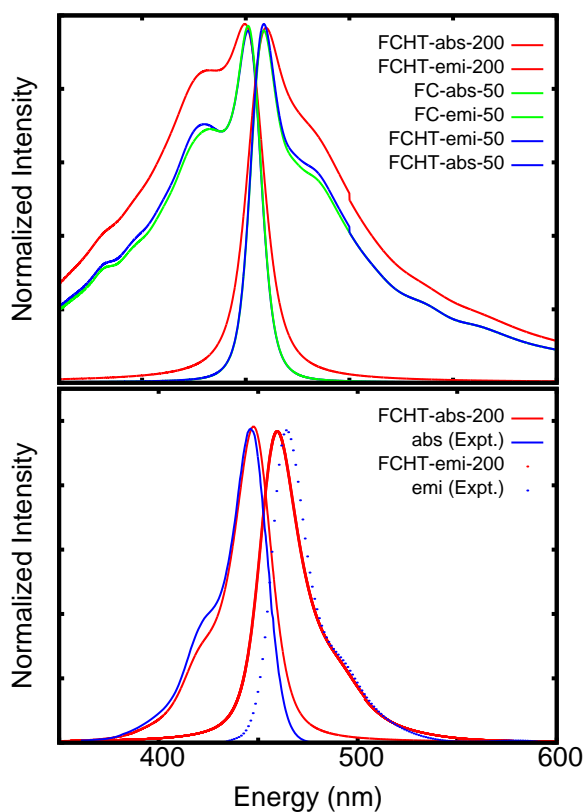


Figure 2: The calculated vibrationaly-resolved absorption (left) and fluorescence (right) spectra at $T = 300.0 \text{ K}$ with different approximations. The top panel: FC and FCHT approximations with inclusion of DR effect at $\gamma = 200$ and 50 cm^{-1} , respectively. The bottom panel: FCHT result with VG approximation at $\gamma = 200 \text{ cm}^{-1}$. For better comparison, the calculated spectra are red-shifted by 6.0 and 15 nm for the results without and with VG approximation, respectively.

configuration change satisfies the condition of harmonic oscillator approximation, ensuring that the subsequent calculations of ISC and RISC rates are effective and reliable.

ISC and RISC rate coefficients

Table 2: The calculated SOCMEs and NAC vectors (NACs) with respect to the geometries of S_1 and T_1 states, respectively.

Transitions	SOCME (cm^{-1})		Transitions	NACs (bohr^{-1})	
	S_1 Geom.	T_1 Geom.		S_1 Geom.	T_1 Geom.
T_1-S_1	0.14	0.15	T_1-T_2	19.50	18.65
T_2-S_1	3.78	4.68	T_1-T_3	7.79	5.69
T_3-S_1	8.92	10.15	T_2-T_3	85.44	214.51
T_1-S_2	13.04	14.30	S_1-S_2	10.61	9.09
T_1-S_3	4.82	3.71	S_1-S_3	19.41	21.09

Table 2 shows that the calculated SOCMEs between S_1 and T_1 are 0.14 and 0.15 cm^{-1} with respect to S_1 and T_1 geometries, respectively, which are negligibly small. The contribution of vibronic coupling effects on the rates of S-T crossings should be significant. Here we thus calculate both the ISC and RISC rates with the inclusion of the FC, HTVC, and DR effects. A result comparison is made with the VG approximation. In our rate calculations, for S_1-T_1 crossings, we set $\Delta E_{S_1T_1} = 1532 \text{ cm}^{-1}$, the experimental energy gap; and for S_1-T_2 crossings, we set $\Delta E_{S_1T_2} = 74 \text{ cm}^{-1}$, the calculated adiabatic energy gap between S_1 and T_2 by TDA-CAM-B3LYP*.

Table 3 shows both the calculated and experimentally-measured rates. For $S_1 - T_1$ crossings, the calculated ISC rates are in the same order of magnitude at $T= 50, 100,$ and 298 K , and the temperature effect on this ISC process is not so evident. The temperature has a larger impact on the RISC rates, which increase obviously with the increase of T at FC approximation. At $T=298 \text{ K}$, the calculated ISC rates are 2.7×10^6 and $4.6 \times 10^7 \text{ s}^{-1}$ with FC and FC+HT approximations, respectively. The HT effect increases the ISC rate by more than one order of magnitude. The calculated results with the VG approximation show the similar tendency. The deviations between the calculated values with and without VG approximation are small, indicating that there is no much large difference between the PESs of two concerned singlet and triplet states. Regardless of

Table 3: The calculated k_{RISC} and k_{ISC} (in unit of s^{-1}) with respect to different approximations and different temperatures T. $\gamma = 20 \text{ cm}^{-1}$ is adopted.

T (K)	without VG approximation		with VG approximation				Expt.
			at S_1 Geom.		at T_1 Geom.		
	FC	HT	FC	HT	FC	HT	
	$k_{S_1 \rightarrow T_1}$						
298	2.7×10^6	4.3×10^7	1.8×10^6	3.8×10^7	1.4×10^6	4.5×10^7	1.5×10^8
100	2.1×10^6	3.6×10^7	1.5×10^6	3.3×10^7	1.1×10^6	4.1×10^7	
50	1.9×10^6	3.5×10^7	1.3×10^6	2.8×10^7	8.4×10^5	2.9×10^7	
	$k_{S_1 \rightarrow T_2}$						
298	6.4×10^8		2.8×10^{10}		6.2×10^9		
100	6.0×10^8		3.8×10^{10}		9.7×10^9		
50	1.7×10^8		3.3×10^{10}		1.0×10^{10}		
	$k_{T_1 \rightarrow S_1}$						
500	2.5×10^4	2.6×10^4	1.0×10^4	2.3×10^4	8.5×10^3	2.0×10^4	6.4×10^3
400	8.7×10^3	2.2×10^4	3.5×10^3	2.2×10^4	2.8×10^3	2.1×10^4	
350	4.2×10^3	2.2×10^4	1.6×10^3	2.2×10^4	1.3×10^3	2.1×10^4	
298	1.5×10^3	2.2×10^4	5.6×10^2	2.2×10^4	4.3×10^2	2.2×10^4	
	$k_{T_2 \rightarrow S_1}$						
500	2.6×10^8		1.0×10^{10}		7.5×10^8		
400	3.2×10^8		1.1×10^{10}		7.9×10^8		
350	3.7×10^8		1.2×10^{10}		8.0×10^8		
298	4.4×10^8		1.3×10^{10}		8.2×10^8		

whether VG approximation is included or not, at room temperature, the contribution of HTVC is much larger than FC. It is thus no doubt that the experimental ISC rate originates predominately from the contribution of the vibronic coupling.

The calculated rate coefficient of $4.6 \times 10^7 \text{ s}^{-1}$ at room temperature is about threefold smaller than the experimentally-measured ISC rate of $1.5 \times 10^8 \text{ s}^{-1}$. This deviation may be attributed to the neglecting of second-order SVC effect in our calculations. To explicitly check the impact of NACs among the low-lying excited states on the rates, we calculated the NAC vectors by the approaches⁷³⁻⁷⁶ implemented within Q-Chem 5.2 package. As Table 2 shows, the calculated NAC vectors are relatively large. The NAC between T_2 and T_3 states even reach 85.44 and 214.51 bohr⁻¹ with respect to S_1 and T_1 geometries, respectively. NACs between the triplet excited states definitely accelerate the ISC.

The theoretical calculations produce much larger ISC and RISC rate coefficients for S_1-T_2 crossing than those for S_1-T_1 crossing because the latter possesses a much smaller energy gap and larger SOCMEs. Considering the NAC vector between T_1-T_2 , we deduce that the population transfer in 7-PhQAD mainly takes place via S_1-T_1 and $S_1-T_2-T_1$.

Concluding remarks

We performed a theoretical study on the geometric and electronic structures, the photophysical properties, and the rate coefficients of the S-T crossings for 7-PhQAD molecule, a newly synthesized MR-type TADF emitter. We found that the HTVC effect on the absorption and fluorescence spectra is negligibly small while it plays a crucial role in the rate coefficients of S-T crossings. The HTVC effect increases the ISC rate by more than one order of magnitude, and when it gets involved, the calculated ISC and RISC rates agree well with the experimental values. Therefore, we conclude that the experimentally-measured ISC rate of 7-PhQAD originates predominantly from the vibronic coupling effects, and the NACs between the triplet excited states play much more important role than those between the singlet ones. It is insufficient to reproduce such a fast experimental ISC rate if only the direct SOC coupling is incorporated because of the larger energy gap of ΔE_{ST} and the negligibly small SOCME between S_1 and T_1 states. The vibronic coupling enhances the population transfer.

However, there exists a small deviation between the calculated and experimental rates, attributed to the neglect of the second-order SVC effect and the inaccurate excited-state PESs produced by the single-reference TDDFT. Like many other MR-type TADF emitters, 7-PhQAD is a strongly correlated electron system. Though its low-lying excited states are single excitation dominated states, more than 10% double excitation characters indicate that the multi-reference quantum chemistry methods are required to exactly describe its excited states. The single-reference TDDFT not only overestimates ΔE_{ST} but also the difference between the PESs of S_1 and S_0 states. The latter results in the significant enhancement of the vibrational motion, leading to the broadband

absorption and emission produced by our theoretical calculation without VG approximation.

This work demonstrates a way to quantitatively predict the ISC and RISC rates of TADF emitters with including the HTVC effect. Our calculations unveil the dynamical mechanism for highly efficient OLED emission and open design routes that go beyond the FC approximation for the future development of high-performance systems.

Acknowledgement

WL thank the financial support from the National Natural Science Foundation of China with grant Nos.21833006 and 2217030161. HM thank the financial support from the Hefei National Laboratory for Physical Sciences at the Microscale with grant No. KF2020103.

Supporting Information Available

The excitation energies of 7-PhQAD calculated by ADC(2)/CC-pVDZ at the S_0 and S_1 geometries, the main geometrical parameters for the ground and excited-state geometries of 7-PhQAD, the charge density difference between the corresponding excited states and ground state by (TD-CAM-B3LYP)*, and the differences between the geometric structures of S_0 and S_1 , of S_0 and T_1 , and between those of S_1 and T_1 optimized at TD-CAM-B3LYP*/6-311++G** level in toluene. The treatment of HT effect in the time-dependent approach and the derivation of damping-related term are provided. This material is available free of charge via the Internet at <http://pubs.acs.org/>.

References

- (1) Tang, C. W.; Vanslyke, S. A. Organic Electroluminescent Diodes. *Appl. Phys. Lett.* **1987**, *51*, 913–915.
- (2) Adachi, C.; Baldo, M. A.; Thompson, M. E.; Forrest, S. R. Nearly 100% Internal Phosphorescence Efficiency in an Organic Light-Emitting Device. *J. Appl. Phys.* **2001**, *90*, 5048–5051.

- (3) Uoyama, H.; Goushi, K.; Shizu, K.; Nomura, H.; Adachi, C. Highly Efficient Organic Light-Emitting Diodes from Delayed Fluorescence. *Nature* **2012**, *492*, 234–238.
- (4) Godumala, M.; Choi, S.; Cho, M. J.; Choi, D. H. Recent Breakthrough in Thermally Activated Delayed Fluorescence Organic Light Emitting Diodes Containing Non-doped Emitting Layer. *J. Mater. Chem. C* **2019**, *7*, 2172–2198.
- (5) Kondo, Y.; Yoshiura, K.; Kitera, S.; Nishi, H.; Hatakeyama, T. Narrowband Deep-Blue Organic Light-Emitting Diode Featuring an Organoboron-Based Emitter. *Nat. Photonics*. **2019**, *13*, 678–682.
- (6) Segal, M.; Baldo, M. A.; Holmes, R. J.; Forrest, S. R.; Soos, Z. G. Excitonic Singlet-Triplet Ratios in Molecular and Polymeric Organic Materials. *Phys. Rev. B* **2003**, *68*, 75211.
- (7) Godumala, M.; Choi, S.; Cho, M. J.; Choi, D. H. Thermally Activated Delayed Fluorescence Blue Dopants and Hosts: From the Design Strategy to Organic Light-Emitting Diode Applications. *J. Mater. Chem. C* **2016**, *4*, 238.
- (8) *Organic Electronics Materials and Devices*; Ogawa, S., Ed.; Springer: Tokyo, 2015.
- (9) Shuai, Z. G.; Peng, Q. Excited States Structure and Processes: Understanding Organic Light-Emitting Diodes at the Molecular Level. *Phys. Rep.* **2014**, *537*, 123–156.
- (10) Shuai, Z. G.; Peng, Q. Organic Light-Emitting Diodes: Theoretical Understanding of Highly Efficient Materials and Development of Computational Methodology. *Natl. Sci. Rev.* **2017**, *4*, 224–239.
- (11) Baryshnikov, G.; Minaev, B.; Ågren, H. Theory and Calculation of the Phosphorescence Phenomenon. *Chem. Rev.* **2017**, *117*, 6500–6537.
- (12) Marian, C. M. Spin-Orbit Coupling Intersystem Crossing in Molecules. *WIREs Comput. Mol. Sci.* **2012**, *2*, 187–203.

- (13) Mchale, J. L. *Molecular spectroscopy*; Pearson College Div: New Haven, Connecticut, USA, 1998.
- (14) Santoro, F.; Lami, A.; Improta, R.; Bloino, J.; Barone, V. Effective Method for the Computation of Optical Spectra of Large Molecules at Finite Temperature Including the Duschinsky and Herzberg-Teller Effect: The Qx Band of Porphyrin as a Case Study. *J. Chem. Phys.* **2008**, *128*, 1724.
- (15) *Computational Strategies for Spectroscopy. From Small Molecules to Nano Systems*; Barone, V., Ed.; Wiley, Ltd.: Chichester, United Kingdom, 2011.
- (16) Spiro, T. G.; Stein, P. Resonance Effects in Vibrational Scattering From Complex Molecules. *Annu. Rev. Phys. Chem.* **1977**, *28*, 501–521.
- (17) Myers, A. B. Resonance Raman Intensities and Charge-Transfer Reorganization Energies. *Chem. Rev.* **1996**, *96*, 911–926.
- (18) Myers, A. B. Resonance Raman Intensity Analysis of Excited-State Dynamics. *Acc. Chem. Res.* **1997**, *30*, 519–527.
- (19) Ma, H. L.; Liu, J.; Liang, W. Z. Time-Dependent Approach to Resonance Raman Spectra Including Duschinsky Rotation and Herzberg-Teller Effects: Formalism and Its Realistic Applications. *J. Chem. Theory Comput.* **2012**, *8*, 4474–4482.
- (20) Liang, W. Z.; Zhao, Y.; Sun, J.; Song, J.; Yang, J. L. Electronic Excitation of Polyfluorenes: A Theoretical Study. *J. Phys. Chem. B* **2006**, *110*, 9908–9915.
- (21) Ma, H. L.; Zhao, Y.; Liang, W. Z. Assessment of Mode-Mixing and Herzberg-Teller Effects on Two-Photon Absorption and Resonance Hyper-Raman Spectra from a Time-Dependent Approach. *J. Chem. Phys.* **2014**, *140*, 94107.

- (22) Liang, W. Z.; Ma, H. L.; Zang, H.; Ye, C. X. Generalized Time-Dependent Approaches to Vibrationally Resolved Electronic and Raman Spectra: Theory and Applications. *Int. J. Quantum Chem.* **2015**, *115*, 550–563.
- (23) Albrecht, A. C. Vibronic Spin-Orbit Perturbations and the Assignment of the Lowest Triplet State of Benzene. *J. Chem. Phys.* **1963**, *38*, 354–365.
- (24) Lim, E. C.; Yu, J. M. H. Vibronic Spin-Orbit Interactions in Heteroaromatic Molecules. II. Phosphorescence of Quinoxaline and Other Diazanaphthalenes. *J. Chem. Phys.* **1968**, *49*, 3878–3884.
- (25) Henry, B. R.; Siebrand, W. Spin-Orbit Coupling in Aromatic Hydrocarbons. Analysis of Nonradiative Transitions between Singlet and Triplet States in Benzene and Naphthalene. *J. Chem. Phys.* **1971**, *54*, 1072–1085.
- (26) Tatchen, J.; Gilka, N.; Marian, C. M. Intersystem Crossing Driven by Vibronic Spin-Orbit Coupling: A Case Study on Psoralen. *Phys. Chem. Chem. Phys.* **2007**, *9*, 5209–5221.
- (27) Etinski, M.; Tatchen, J.; Marian, C. M. Time-Dependent Approaches for the Calculation of Intersystem Crossing Rates. *J. Chem. Phys.* **2011**, *134*, 154105.
- (28) Etinski, M.; Rai-Constapel, V.; Marian, C. M. Time-Dependent Approach to Spin-Vibronic Coupling: Implementation and Assessment. *J. Chem. Phys.* **2014**, *140*, 114104.
- (29) Peng, Q.; Niu, Y.; Shi, Q.; Gao, X.; Shuai, Z. G. Correlation Function Formalism for Triplet Excited State Decay: Combined Spin-Orbit and Nonadiabatic Couplings. *J. Chem. Theory Comput.* **2013**, *9*, 1132–1143.
- (30) Gibson, J.; Monkman, A. P.; Penfold, T. J. The Importance of Vibronic Coupling for Efficient Reverse Intersystem Crossing in Thermally Activated Delayed Fluorescence Molecules. *ChemPhysChem* **2016**, *17*, 2956–2961.

- (31) Penfold, J. T.; Gindensperger, E.; Daniel, C.; Marian, C. M. Spin-Vibronic Mechanism for Intersystem Crossing. *Chem. Rev.* **2018**, *118*, 6975–7025.
- (32) Föllner, J.; Marian, C. M. Rotationally Assisted Spin-State Inversion in Carbene-Metal-Amides Is an Artifact. *J. Phys. Chem. Lett.* **2017**, *8*, 5643–5647.
- (33) Kim, I.; Jeon, S. O.; Jeong, D.; Choi, H.; Lee, H. S. Spin-Vibronic Model for Quantitative Prediction of Reverse Intersystem Crossing Rate in Thermally Activated Delayed Fluorescence Systems. *J. Chem. Theory Comput.* **2020**, *16*, 621–632.
- (34) Ou, Q.; Peng, Q.; Shuai, Z. G. Toward Quantitative Prediction of Fluorescence Quantum Efficiency Through Combining Direct Vibrational Conversion and Surface Crossing: BODIPYs as Example. *J. Phys. Chem. Lett.* **2020**, *11*, 7790–7797.
- (35) Peng, Q.; Fan, D.; Duan, R.; Yi, Y.; Niu, Y.; Wang, D.; Shuai, Z. G. Theoretical Study of Conversion and Decay Processes of Excited Triplet and Singlet States in a Thermally Activated Delayed Fluorescence Molecule. *J. Phys. Chem. C* **2017**, *121*, 13448–13456.
- (36) Li, X.; Shi, Y. Z.; Wang, K.; Zhang, M.; Zheng, C. J.; Sun, D. M.; Dai, G. L.; Fan, X. C.; Wang, D. Q.; Liu, W.; Li, J., Y. Q. and Yu; Ou, X. M.; Adachi, C.; Zhang, X. H. Thermally Activated Delayed Fluorescence Carbonyl Derivatives for Organic Light-Emitting Diodes with Extremely Narrow Full Width at Half-Maximum. *ACS Appl. Mater. Interfaces* **2019**, *11*, 13472–13480.
- (37) El-sayed, M. A. Spin-Orbit Coupling and the Radiationless Processes in Nitrogen Heterocyclics. *J. Chem. Phys.* **1963**, *38*, 2834–2838.
- (38) Herzberg, G. *Electronic Spectra and Electronic Structure of Polyatomic Molecules*; Van Nostrand: Princeton, NJ, 1967.
- (39) Duschinsky, F. On the Interpretation of Electronic Spectra of Polyatomic Molecules I: The Franck-Condon principle. *Acta. Phys-Chim. URSS* **1937**, *7*, 551.

- (40) Ferrer, F. J. A.; Barone, V.; Cappelli, C.; Santoro, F. Duschinsky, Herzberg-Teller, and Multiple Electronic Resonance Interferential Effects in Resonance Raman Spectra and Excitation Profiles. The Case of Pyrene. *J. Chem. Theory Comput.* **2013**, *9*, 3597–3611.
- (41) Valiev, R. R.; Cherepanov, V. N.; Nasibullin, R. T.; Sundholm, D.; and Kurten, T. Calculating Rate Constants for Intersystem Crossing and Internal Conversion in the Franck-Condon and Herzberg-Teller Approximations. *Phys. Chem. Chem. Phys.* **2019**, *21*, 18495-18500 .
- (42) Patil, V. V.; Lee, H. L.; Kim, I.; Lee, K. H.; Chung, W. J.; Kim, J.; Park, S.; Choi, H.; Son, W.; Jeon, S. O; and Lee, J. Y. Purely Spin-Vibronic Coupling Assisted Triplet to Singlet Up-Conversion for Real Deep Blue Organic Light-Emitting Diodes with Over 20% Efficiency and y Color Coordinate of 0.05. *Adv. Sci.* **2021**, 2101137.
- (43) Chen, X.; Zhang, S.; Fan, J.; Ren, A. M Nature of Highly Efficient Thermally Activated Delayed Fluorescence in Organic Light-Emitting Diode Emitters: Nonadiabatic Effect between Excited States. *J. Phys. Chem. C* **2015**, *119*, 9728 .
- (44) Feshbach, H. *Quantum Mechanics.*; American Association for the Advancement of Science: New York, 1962.
- (45) Lawetz, V.; Orlandi, G.; Siebrand, W. Theory of Intersystem Crossing in Aromatic Hydrocarbons. *J. Chem. Phys.* **1972**, *56*, 4058–4072.
- (46) Mukamel, S. *The Principles of Nonlinear Optical Spectroscopy*; Oxford University Press: New York, 1995.
- (47) Shao, Y. H.; Gan, Z. T.; Epifanovsky, E.; Gilbert, A. T. B.; Wormit, M.; Kussmann, J.; Lange, A. W.; Behn, A.; Deng, J.; Feng, X. T.; Ghosh, D.; Goldey, M.; Horn, P. R.; Jacobson, L. D.; Kaliman, I.; Khaliullin, R. Z.; Kus, T.; Landau, A.; Liu, J.; Proynov, E. I.; Rhee, Y. M.; Richard, R. M.; Rohrdanz, M. A.; Steele, R. P.; Sundstrom, E. J.; Woodcock, H. L.; Zimmerman, P. M.; Zuev, D.; Albrecht, B.; Alguire, E.; Austin, B.; Beran, G. J. O.; Bernard,

Y. A.; Berquist, E.; Brandhorst, K.; Bravaya, K. B.; Brown, S. T.; Casanova, D.; Chang, C. M.; Chen, Y. Q.; Chien, S. H.; Closser, K. D.; Crittenden, D. L.; Diedenhofen, M.; DiStasio, R. A.; H. Do, Dutoi, A. D.; Edgar, R. G.; Fatehi, S.; Fusti-Molnar, L.; Ghysels, A.; Golubeva-Zadorozhnaya, A.; Gomes, J.; Hanson-Heine, M. W. D.; Harbach, P. H. P.; Hauser, A. W.; Hohenstein, E. G.; Holden, Z. C.; Jagau, T. C.; Ji, H. J.; Kaduk, B.; Khistyayev, K.; Kim, J.; Kim, J.; King, R. A.; Klunzinger, P.; Kosenkov, D.; Kowalczyk, T.; Krauter, C. M.; Lao, K. U.; Laurent, A. D.; Lawler, K. V.; Levchenko, S. V.; Lin, C. Y.; Liu, F.; Livshits, E.; Lochan, R. C.; Luenser, A.; Manohar, P.; Manzer, S. F.; Mao, S. P.; Mardirossian, N.; Marenich, A. V.; Maurer, S. A.; Mayhall, N. J.; Neuscamman, E.; Oana, C. M.; Olivares-Amaya, R.; O'Neill, D. P.; Parkhill, J. A.; Perrine, T. M.; Peverati, R.; Prociuk, A.; Rehn, D. R.; Rosta, E.; Russ, N. J.; Sharada, S. M.; Sharma, S.; Small, D. W.; Sodt, A.; Stein, T.; Stuck, D.; Su, Y. C.; Thom, A. J. W.; Tsuchimochi, T.; Vanovschi, V.; Vogt, L.; Vydrov, O.; Wang, T.; Watson, M. A.; Wenzel, J.; White, A.; Williams, C. F.; Yang, J.; Yeganeh, S.; Yost, S. R.; You, Z. Q.; Zhang, I. Y.; Zhang, X.; Zhao, Y.; Brooks, B. R.; Chan, G. K. L.; Chipman, D. M.; Cramer, C. J.; Goddard, W. A.; Gordon, M. S.; Hehre, W. J.; Klamt, A.; Schaefer, H. F.; Schmidt, M. W.; Sherrill, C. D.; Truhlar, D. G.; Warshel, A.; Xu, X.; Aspuru-Guzik, A.; Baer, R.; Bell, A. T.; Besley, N. A.; Chai, J. D.; Dreuw, A.; Dunietz, B. D.; Furlani, T. R.; Gwaltney, S. R.; Hsu, C. P.; Jung, Y. S.; Kong, J.; Lambrecht, D. S.; Liang, W. Z.; Ochsenfeld, C.; Rassolov, V. A.; Slipchenko, L. V.; Subotnik, J. E.; Van Voorhis, T.; Herbert, J. M.; Krylov, A. I.; Gill, P. M. W.; Head-Gordon, M. Advances in Molecular Quantum Chemistry Contained in the Q-Chem 4 Program Package. *Mol. Phys.* **2014**, *113*, 184–215.

- (48) Hirata, S.; Sakai, Y.; Masui, K.; Tanaka, H.; Adachi, C. Highly Efficient Blue Electroluminescence Based on Thermally Activated Delayed Fluorescence. *Nat. Mater.* **2014**, *14*, 330–336.
- (49) Dias, F. B.; Penfold, T. J.; Monkman, A. P. Photophysics of Thermally Activated Delayed Fluorescence Molecules. *Methods Appl. Fluoresc.* **2017**, *5*, 012001.
- (50) Wong, M. Y.; Zysman-Colman, E. Purely Organic Thermally Activated Delayed Fluorescence

- Materials for Organic Light-Emitting Diodes. *Adv. Mater.* **2017**, *29*, 1605444.
- (51) Penfold, T. J.; Dias, F. B.; Monkman, A. P. The Theory of Thermally Activated Delayed Fluorescence for Organic Light Emitting Diodes. *Chem. Commun.* **2018**, *54*, 3926–3935.
- (52) *Highly Efficient OLEDs with Phosphorescent Materials*; Yersin, H., Ed.; Wiley-VCH: Weinheim, 2008.
- (53) Korzdorfer, T.; Sears, J. S.; Sutton, C.; Bredas, J. L. Long-Range Corrected Hybrid Functionals for π -Conjugated Systems: Dependence of the Range-Separation Parameter on Conjugation Length. *J. Chem. Phys.* **2011**, *135*, 204107.
- (54) Sun, H. T.; Zhong, C.; Sun, Z. R. Recent Advances in the Optimally "Tuned" Range-Separated Density Functional Theory. *Acta. Phys-Chim. Sin.* **2016**, *32*, 2197–2208.
- (55) Stein, T.; Kronik, L.; Baer, R. Reliable Prediction of Charge Transfer Excitations in Molecular Complexes Using Time-Dependent Density Functional Theory. *J. Am. Chem. Soc.* **2009**, *131*, 2818–2820.
- (56) Tu, C. Y.; Liang, W. Z. NB-Type Electronic Asymmetric Compounds as Potential Blue-Color TADF Emitters: Steric Hindrance, Substitution Effect, and Electronic Characteristics. *ACS Omega* **2017**, *2*, 3098–3109.
- (57) Tu, C. Y.; Liang, W. Z. Benzazasiline Combined with Triphenylborane-Based Cores for Constructing Deep-Blue Donor-Acceptor-Donor TADF Emitters. *Org. Electron.* **2018**, *57*, 74–81.
- (58) Kronik, L.; Stein, T.; Refaelyabramson, S.; Baer, R. Excitation Gaps of Finite-Sized Systems from Optimally Tuned Range-Separated Hybrid Functionals. *J. Chem. Theory Comput.* **2012**, *8*, 1515–1531.
- (59) Sun, H.; Zhong, C.; Bredas, J. Reliable Prediction with Tuned Range-Separated Functionals of the Singlet-Triplet Gap in Organic Emitters for Thermally Activated Delayed Fluorescence. *J. Chem. Theory Comput.* **2015**, *11*, 3851–3858.

- (60) Miertuš, S.; Scrocco, E.; Tomasi, J. Electrostatic Interaction of a Solute with a Continuum. A Direct Utilization of Ab Initio Molecular Potentials for the Prediction of Solvent Effects. *Chem. Phys.* **1981**, *55*, 117–129.
- (61) Miertuš, S.; Tomasi, J. Approximate Evaluations of the Electrostatic Free Energy and Internal Energy Changes in Solution Processes. *Chem. Phys.* **1982**, *65*, 239–245.
- (62) Cammi, R.; Mennucci, B.; Tomasi, J. Fast Evaluation of Geometries and Properties of Excited Molecules in Solution: A Tamm-Dancoff Model with Application to 4-Dimethylaminobenzonitrile. *J. Phys. Chem. A* **2000**, *104*, 5631–5637.
- (63) Hirata, S.; Head-Gordon, M. Time-dependent Density Functional Theory Within the Tamm-Dancoff Approximation. *Chem. Phys. Lett.* **1999**, *314*, 291–299.
- (64) Lu, T.; Chen, F. W. Multiwfn: A Multifunctional Wavefunction Analyzer. *J. Comput. Chem.* **2012**, *33*, 580–592.
- (65) Liu, Z. Y.; Lu, T.; Chen, Q. X. An Sp-Hybridized All-Carboatomic Ring, Cyclo[18]Carbon: Electronic Structure, Electronic Spectrum, and Optical Nonlinearity. *Carbon* **2020**, *165*, 461–467.
- (66) Stephens, P. J.; Devlin, F. J.; Chabalowski, C. F.; Frisch, M. J. Ab Initio Calculation of Vibrational Absorption and Circular Dichroism Spectra Using Density Functional Force Fields. *J. Phys. Chem.* **1994**, *98*, 247–257.
- (67) Yanai, T.; Tew, D. P.; Handy, N. C. A New Hybrid Exchange-Correlation Functional Using the Coulomb-Attenuating Method (CAM-B3LYP). *Chem. Phys. Lett.* **2004**, *393*, 51–57.
- (68) Leininger, T.; Stoll, H.; Werner, H. J.; Savin, A. Combining Long-Range Configuration Interaction with Short-Range Density Functionals. *Chem. Phys. Lett.* **1997**, *275*, 151–160.
- (69) Chai, J. D.; Head-Gordon, M. Long-Range Corrected Hybrid Density Functionals with

- Damped Atom-Atom Dispersion Corrections. *Phys. Chem. Chem. Phys.* **2008**, *10*, 6615–6620.
- (70) Ai, W.; Fang, W. H.; Su, N. Q. The Role of Range-Separated Correlation in Long-Range Corrected Hybrid Functionals. *J. Phys. Chem. Lett.* **2021**, *12*, 1207–1213.
- (71) Wenzel, J.; Wormit, M.; and Dreuw, A. Calculating X-ray Absorption Spectra of Open-Shell Molecules with the Unrestricted Algebraic-Diagrammatic Construction Scheme for the Polarization Propagator. *J. Chem. Theory Comput.* **2014**, *10*, 4583–4598. .
- (72) Santoro, F.; Cappelli, C.; Barone, V. Effective Time-Independent Calculations of Vibrational Resonance Raman Spectra of Isolated and Solvated Molecules Including Duschinsky and Herzberg-Teller Effects. *J. Chem. Theory Comput.* **2011**, *7*, 1824–1839.
- (73) Fatehi, S.; Alguire, E.; Shao, Y. H.; Subotnik, J. E. Analytic Derivative Couplings between Configuration-Interaction-Singles States with Built-in Electron-Translation Factors for Translational Invariance. *J. Chem. Phys.* **2011**, *135*, 234105.
- (74) Zhang, X.; Herbert, J. M. Analytic Derivative Couplings for Spin-Flip Configuration Interaction Singles and Spin-Flip Time-Dependent Density Functional Theory. *J. Chem. Phys.* **2014**, *141*, 64104.
- (75) Ou, Q.; Bellchambers, G. D.; Furche, F.; Subotnik, J. E. First-Order Derivative Couplings between Excited States from Adiabatic TDDFT Response Theory. *J. Chem. Phys.* **2015**, *142*, 64114.
- (76) Zhang, X.; Herbert, J. M. Analytic Derivative Couplings in Time-Dependent Density Functional Theory: Quadratic Response Theory Versus Pseudo-Wavefunction Approach. *J. Chem. Phys.* **2015**, *142*, 64109.